Fast-beam laser lifetime measurements of the cesium $6p\,^2P_{1/2,3/2}$ states

Robert J. Rafac,* Carol E. Tanner, A. Eugene Livingston, and H. Gordon Berry
Department of Physics, University of Notre Dame, 225 Nieuwland Science Hall, Notre Dame, Indiana 46556-5670
(Received 7 August 1998; revised manuscript received 6 August 1999)

We provide a detailed description of our fast-beam laser lifetime measurements in atomic cesium. Selective excitation of the neutral ^{133}Cs $6p\,^2P_{1/2}$ and $6p\,^2P_{3/2}$ states is accomplished with resonant diode laser light directed transversely to the atomic velocity. The in-flight decay of the excited-state fluorescence is observed with a position-correlated single photon-counting detector. The Doppler-shifted $6p\,^2P_{3/2}$ resonance, when probed with longitudinally propagating laser radiation, provides a precise means for determination of the beam velocity, and converts the position scale to a time scale. Our lifetime results are 35.07 ± 0.10 ns for the $6p\,^2P_{1/2}$ state and 30.57 ± 0.07 ns for the $6p\,^2P_{3/2}$ state. These results represent a data set larger than in our previous work, and include beam divergence corrections which have been evaluated by two different methods. We present comparisons of our results with previous measurements and with relativistic many-body calculations of atomic transition matrix elements in this neutral alkali system. [S1050-2947(99)09711-5]

PACS number(s): 32.70.Fw, 32.70.Cs, 32.70.Jz, 34.90.+q

I. INTRODUCTION

Laser excitation of a fast atomic beam is an extremely versatile technique for the measurement of atomic lifetimes applicable to a variety of ionic and neutral systems [1]. This technique provides an exceptional combination of excitation selectivity, intense fluorescence unaffected by collisions or radiation trapping, and a precise spatial time scale. Early fast-beam laser measurements in light atoms [2] indicated the possibility of reaching uncertainties below 0.2%. However, recent fast-beam laser measurements [3] suggested the presence of an unaccounted for systematic error in Ref. [2]. The work presented here uses an alternative approach for measuring the atomic beam velocity [4,5].

Our measurements are motivated by their relationship to the interpretation of parity nonconservation (PNC) in atomic systems which arises from the modification of the atomic structure by the weak interaction [6]. Recent measurements carried out by Wood and co-workers [7,8] place a 0.35% uncertainty on the PNC asymmetry in the neutral cesium $6s\,^2S_{1/2}\rightarrow 7s\,^2S_{1/2}$ transition. The interpretation of these results in terms of the weak interaction requires accurate knowledge of the atomic structure including radial matrix elements and transition energies. Of greatest importance are the low lying $np\,^2P$ states which couple to the $6s\,^2S_{1/2}$ and $7s\,^2S_{1/2}$ states through parity-odd interactions. In this paper, we report fast-beam laser lifetime measurements of the cesium $6p\,^2P_{1/2,3/2}$ states. The $6p\,^2P$ states are of special interest because they decay only to the $6s\,^2S_{1/2}$ ground state, and therefore the lifetime measurements provide direct knowledge of the reduced radial matrix elements via the well-known expression for isotropic spontaneous emission into three dimensions:

$$\frac{1}{\tau_J}=A_J=\frac{4}{3}\alpha\frac{\omega_J^3}{c^2}\frac{|\langle 6p\,^2P_J||r||6s\,^2S_{1/2}\rangle|^2}{2J+1}, \tag{1}$$

where τ_J is the lifetime of the $6p\,^2P_J$ state, A_J is the transition probability for spontaneous emission, ω_J is the transition frequency, c is the speed of light, and α is the fine structure constant. In addition to testing directly the accuracy of high-precision atomic structure calculations, these matrix elements provide the calibration for other transition strength measurements in cesium which are an important part of our research efforts [9].

Our lifetime measurements are performed using perpendicular laser excitation resonant with the $6s\,^2S_{1/2}\rightarrow 6p\,^2P_{1/2,3/2}$ transitions in a fast neutral cesium beam, combined with detection of the in-flight decay of the subsequent beam fluorescence. The spatial decay signal is converted into a temporal decay curve using a precise velocity measurement of the neutral beam. This velocity measurement relies on the wavelength comparison between the longitudinally excited resonance in the fast beam and the resonance in a thermal vapor cell at rest in the laboratory. Figure 1 shows the relevant atomic states and transition wavelengths.

If an ensemble of N_J atoms in an excited state J at time t_0 decays by spontaneous emission, the population obeys the rate equation

$$N_J(t)=N_J(t_0)e^{-(t-t_0)/\tau_J}. \tag{2}$$

where the lifetime τ_J is given in terms of the atomic structure by Eq. (1). The detected fluorescence intensity due to spontaneous emission, $I(t)$, is proportional to the population rate of change, i.e.,

$$I(t)=I(t_0)e^{-(t-t_0)/\tau_J}. \tag{3}$$

In the case of an ensemble of atoms moving with speed v, the spatial dependence of the fluorescence intensity is simply

$$I(z)=I(z_0)e^{-(z-z_0)/v\tau_J}. \tag{4}$$

The lifetime τ_J can thus be determined through fitting the observed fluorescence signal to Eq. (4). An excellent earlier survey of a variety of atomic lifetime measurement techniques is given by Imhof and Read in Ref. [10]. A more

*Present address: Time and Frequency Division, National Institute of Standards and Technology, 325 Broadway, Boulder, CO 80303.

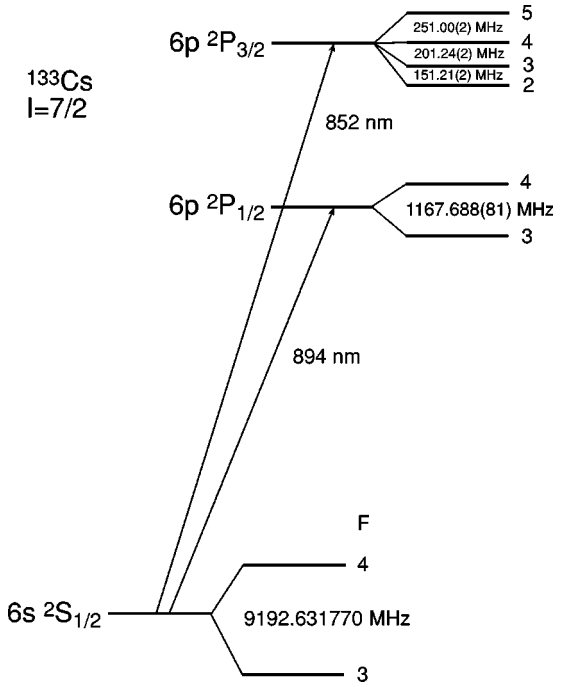

FIG. 1. Atomic states with hyperfine intervals [31,32,38] and rest frame transition wavelengths. Longitudinal excitation redshifts the resonances by about 10.6 cm^{-1}.

detailed and up-to-date review pertaining to accelerator based methods including the one used here can be found in Ref. [11].

II. FAST NEUTRAL BEAM PRODUCTION

A. Ion beam

Singly charged cesium ions are produced from a heated CsCl sample in an ion source of the ''oscillating-electron'' type first constructed by Sidenius and Nielsen [12]. This source is capable of producing up to 1 mA of total ion current with an energy spread of <50 eV and a half-angle of divergence of 70 mrad at 5 kV. In our source oven, we use granular CsCl at an oven temperature of 775 K. Positive ions are extracted from the source at a kinetic energy of approximately 10 kV. The resulting ion beam is focused with an electrostatic lens (≈ 2.5 kV) and accelerated through an additional potential of 40 kV. The largest component of high-voltage noise occurs at 120 Hz. This ripple is electronically suppressed below 0.2 V peak to peak with a negative feedback servo amplifier [13]. The resulting fast ion beam is monoenergetic to four parts in 10^6. The source output is momentum analyzed in a 90° bending magnet, and the resulting beam consists solely of 50-keV Cs^+ ions. The beam is focused with a magnetic quadrupole lens and electrostatically steered toward the measurement area.

B. Neutralization

To obtain a neutral Cs beam, we recombine the ions via near-resonant charge exchange in a rubidium vapor target mounted 2 m upstream from the target chamber. The beam ions traverse 7.5 cm of Rb vapor (density $\approx 3\times 10^{13}$ cm^{-3}), and fast neutral cesium atoms emerge from the cell as a result of the following process:

$$Cs^+(+50\ \text{keV}) + Rb \rightarrow Cs(+50\ \text{keV} - 0.28\ \text{eV}) + Rb^+. \quad (5)$$

The Rb^+ ions eventually neutralize during wall collisions and/or leave the apparatus. This near resonant process has a relatively large cross section (of order 10^{-15} cm^2 at 50 keV) [14] because the ionization potentials of the two neutral species differ by only 0.28 eV. The neutralization process is typically $>90\%$ efficient as determined through measurements of the ion intensity via an electrostatic analyzer and Faraday cup. Apertures in the beam line before and after the charge-exchange cell restrict Rb vapor from effusing throughout the system, and a diffusion pump immediately beneath the cell captures the vapor. Two sets of scanning beam-profile monitors and three apertures connected to charge integrators provide diagnostic information for beam steering and quality assessment. By steering the ions out of the beam, the flux of neutrals and ions are each measured separately.

III. TARGET CHAMBER

Our lifetime apparatus is mounted to the inside lid of a vacuum chamber with the atomic beam travelling parallel to the lid 9.5 cm below the inner surface. Linearly polarized laser light enters the excitation region through a Brewster window, and intersects the atomic beam at right angles. A mirror retroreflects the laser light back through the atomic beam and out of the chamber. The laser is tuned to populate the desired upper state, and is polarized parallel to the atomic beam direction. A light shield separates the excitation region from the detection region. Figure 2 shows side and plan views of the apparatus.

The excited atoms decay in flight via spontaneous emission, and the decay fluorescence is collected by three polarization insensitive glass-fiber bundles oriented transversely to the atomic beam. The packing fraction (0.85) and core refractive index (1.58) yield an incident-light capture efficiency of 70%. Optical feedthroughs [15] couple the collected light out of the vacuum chamber with a signal loss of about 40% into an external set of bundles. Over the entire 1.3-m length of the coupled bundles, 30% of the light is lost to attenuation.

One bundle, mounted 2.75 cm downstream from the excitation point, provides the ''t_0'' normalization of the fluorescence decay, and corrects to first order for atomic beam and laser intensity fluctuations. An additional light shield protects this fiber bundle from scattered light generated in the excitation region. The two remaining fiber bundles, mounted in an aluminum block with a 6-mm hole, view the atomic beam from opposite sides. A precision lead screw driven with a stepper motor translates the detector block for observation of the fluorescence decay as a function of position. The motor operates under computer control and can translate the bundles with a resolution of 1.5875×10^{-3} mm/motor pulse over a 10.4-cm range.

The external fiber bundles carry the light to two photomultipliers chosen for their high responsivity in the infrared. To limit thermal dark pulses, these tubes are operated at -30°C. Narrow-band interference filters prevent nonresonant background light from entering the phototubes. Sig-

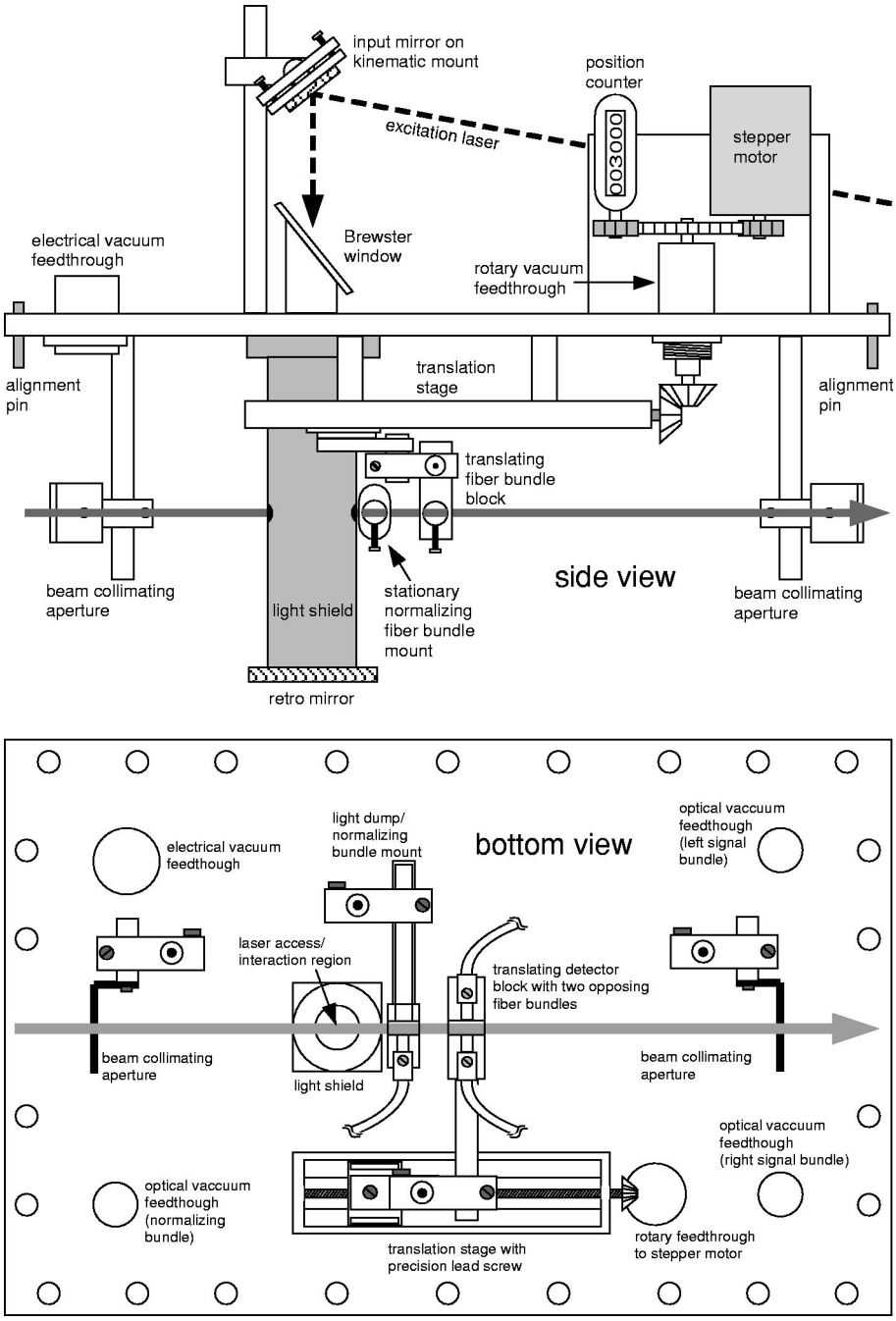

FIG. 2. Side and bottom views of the lifetime apparatus as mounted on the chamber lid. For clarity, the optical fiber feedthroughs and mu-metal enclosure are not shown.

nal rates are maintained in the single-photon counting regime.

Two apertures on the lid are used to measure ion beam currents (3.2-mm diameter before the interaction region and 3.5-mm diameter after the detection region). The current measurements provide beam steering and diagnostic information. The charge exchange cell aperture (3.2-mm diameter) and the first lid aperture (3.2-mm diameter), which are separated by 2.0 m, define the atomic beam direction.

The presence of magnetic fields in the chamber volume could induce quantum beats between closely spaced Zeeman sublevels. We suppress these effects by lining the chamber with magnetic shielding and by using a polarization insensitive detection system. In addition, no magnetic materials are used near the interaction region of the apparatus. A Hall-probe-type gaussmeter measures a vertical field component of 0.046 G in the decay region and a horizontal component that varies somewhat with position, from 0.03 to 0.04 G.

IV. DIODE LASERS

Diode lasers are especially suited for this measurement because of their intensity stability and availability at the desired wavelengths. We employ commercial semiconductor laser diodes enclosed in temperature-controlled housings of our own design [15]. For these measurements, our diode lasers are operated in a free-running mode with a single-mode spectral bandwidth of approximately 40 MHz. Transit time broadening contributes approximately 100 MHz to the resonance width, and the transverse angular spread of the atomic beam produces an additional 1 GHz of inhomogeneous broadening. The upper-state hyperfine levels are therefore

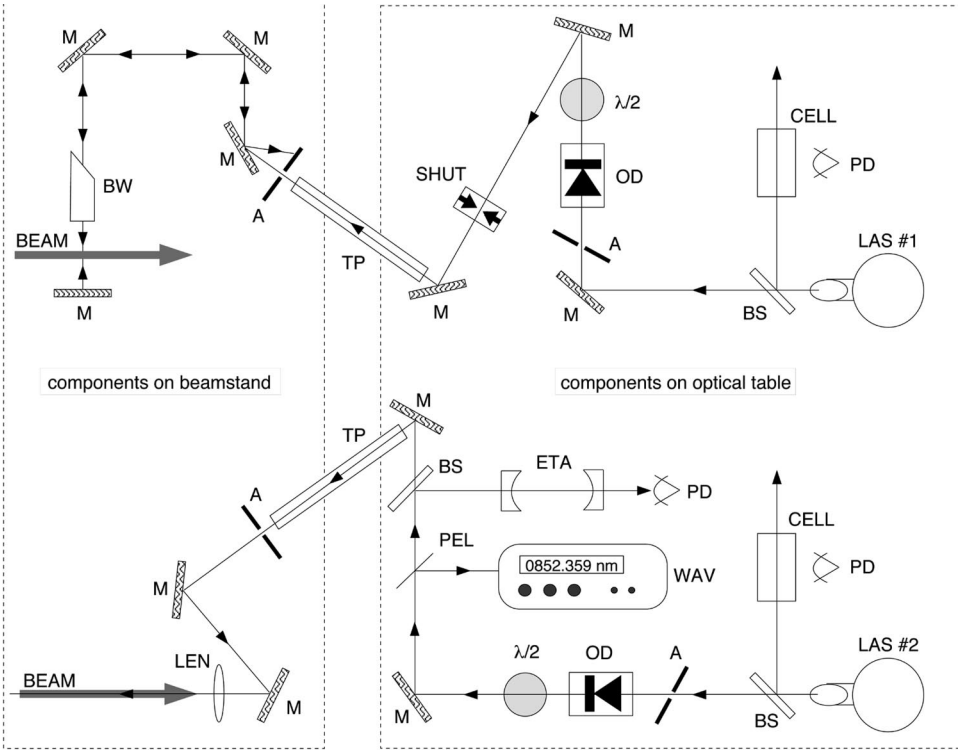

FIG. 3. Complete laser map for lifetime measurements. The two laser sources LAS and associated optics are located on an optical table, and light for excitation and the velocity probe is sent through a transport pipe TP to the beamstand for measurements. Other components: BS, beamsplitter; CELL, Cs vapor cell; PD, photodiode detector; A, aperture; M, gold first-surface mirror; OD, optical diode; λ/2, half-wave retarder; SHUT, computer controlled shutter; PEL, pellicle beamsplitter; WAV, scanning wavemeter; ETA, scanning confocal etalon; BW, Brewster window; LEN, focusing lens.

non-selectively populated during perpendicular excitation. For the $6p\,^2P_{3/2}$ state, we use a single-mode diode selected for its wavelength, 852 nm, and high output power of >50 mW. To populate the $6p\,^2P_{1/2}$ state, we selected a single-mode diode laser at 894 nm with an output power of 8 mW. With these power levels, we do not observe saturation of the decay fluorescence signal, and the signal increases more rapidly than the background. We therefore endeavor to use the maximum power available from each laser in order to minimize our sensitivity to the background. The laser sources are mounted on an optical table with the associated steering optics and optical diodes to isolate the diode lasers from backscattered light which adversely affects the tuning properties. Cesium vapor cells and an optical spectrum analyzer are used for laser tuning, diagnostics, and wavemeter calibration; see Fig. 3.

V. VELOCITY MEASUREMENT

A number of approaches have been used to measure fast-beam velocities. One of the most straightforward methods involves measuring the acceleration voltage to obtain the velocity of the ions. This approach requires a precisely calibrated voltage divider capable of withstanding the high potentials involved. Andrä *et al.* employed this technique [1], and calibrated the voltage using known nuclear reactions with an uncertainty of $\pm 1\%$. However, as demonstrated by Volz and co-workers [16,17], the actual kinetic energy of the ions depends on the operating conditions of the source (e.g., extraction voltage) which limits the accuracy of this method. In another experiment, Andrä *et al.* used an electrostatic analyzer to determine the ion velocities from their trajectories in a radial electric field [2]. Uncertainty in the geometry of the device limited the velocity uncertainty to about $\pm 0.2\%$ in this case.

Both of these methods suffer from the difficulty that only the *ionic* velocities are measured, and neutral atom velocities can differ from those of the ion. An obvious mechanism for an energy difference is the charge exchange process. Volz and co-workers demonstrated an energy loss using an electrostatic analyzer to evaluate the difference between the accelerating voltage and the ion-beam energy after neutralization and reionization with two charge exchange cells. In their neutral atom lifetime experiments [16,17], they assumed the kinetic energy lost after a single charge exchange to be half that for the combined processes. With this procedure, they inferred the neutral atom velocity from measurements of the accelerating voltage with a quoted precision of $\pm 0.04\%$.

To measure the neutral atom velocity directly, we employ a third technique demonstrated by Koch [18] which involves observing a Doppler-shifted resonance transition in the fast atomic beam. This method works equally well for both ions and neutrals, and can probe both populations independently. Using a third diode laser, we observe the $6s\,^2S_{1/2} \rightarrow 6p\,^2P_{3/2}$ resonance $(D2)$ with collinear counterpropagating laser radiation. The laser enters a window at the downstream end of the beamline, overlaps the atomic beam path, and exits a second window near the 90° analyzing magnet. The laser beam comes to a focus near the charge exchange cell, and a third photomultiplier detects this fluorescence 30 cm downstream (see Fig. 4). The frequency ω_L' of the laser in the rest frame of a fast atom is given by the Doppler shift expression

$$\omega_L' = \omega_L \frac{1-\beta}{\sqrt{1-\beta^2}}, \tag{6}$$

where ω_L is the laser frequency in the laboratory frame, and β is the velocity of the atoms in the laboratory frame divided by the speed of light. A collinear probe laser is advantageous

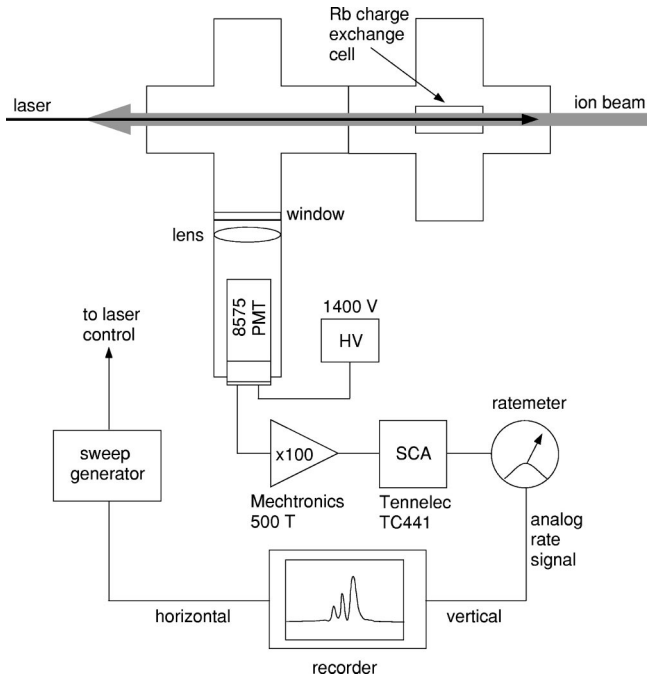

FIG. 4. Resonance fluorescence detection setup for velocity measurement. The counterpropagating probe laser enters the beamline upstream on the left, and the fluorescence is detected as a function of laser frequency.

because transit time broadening is minimized, and the uncertainty due to angular misalignment between atomic and laser beams is eliminated to first order. For a 50-keV cesium beam and a counterpropagating probe laser, the $D2$ resonance line appears redshifted by approximately 10.6 cm^{-1} in the laboratory frame. A commercial scanning wavemeter determines the wavelength with a precision of 0.01 cm^{-1}. Because of velocity-group compression resulting from electrostatic acceleration, the excited-state hyperfine splittings are clearly resolved as shown in Fig. 5. The spectral resolution is limited primarily by the 40-MHz finite linewidth of the free-running diode laser.

VI. DATA ACQUISITION AND CONTROL

The data-acquisition system is illustrated in Fig. 6. Two phototubes are operated with a cathode bias of -1.6 kV, and the anode output pulses are amplified 100 times, each through two channels of a quad fast amplifier with rise and fall times of <3 ns and a bandwidth of >120 MHz. Discriminators veto thermal noise at levels determined by comparing pulse-height spectra of the dark noise with spectra in the presence of signal for each tube. With the phototubes at $-30\,^{\circ}$C and a small amount of amplitude discrimination, the dark noise contribution to the count rate is typically on the order of 100 Hz in both the normalization and signal channels. For a typical beam current of 2.5 μA, total count rates of tens of kHz in both the normalizing and detection channels are obtained. With the laser shutter both opened and closed, observations are recorded at 31 positions of the translating detector block. When measuring the dark count rate, a delay of 650 ms is introduced into the acquisition timing after the laser shutter is closed. This procedure eliminates artificial changes in dark counts that depend on the recent counting history of the tubes.

Table I summarizes the typical operating parameters, beam currents, and signal sizes. A number of factors reduce the $6p\,^2P_{1/2}$ fluorescence signal compared to that of the $6p\,^2P_{3/2}$ state. First, the available laser power at 894 nm is only about 15% of that available at 852 nm. Second, the quantum efficiency of the photomultipliers drops rapidly in the near infrared, and is about a factor of three smaller at 894 nm as compared with 852 nm.

VII. MEASUREMENT PROTOCOL

The data described below include 68 translation sweeps of the moving detector, each taking about 11 min with the majority of the time spent on the $6p\,^2P_{1/2}$ decay which has an intrinsically lower counting rate. Groups of 12 scans of the fluorescence decay are taken with the cesium beam on target, six with the detector translating downstream relative to the beam, and six translating upstream. The translating detector counts photons for 10 s at each of 31 positions along the

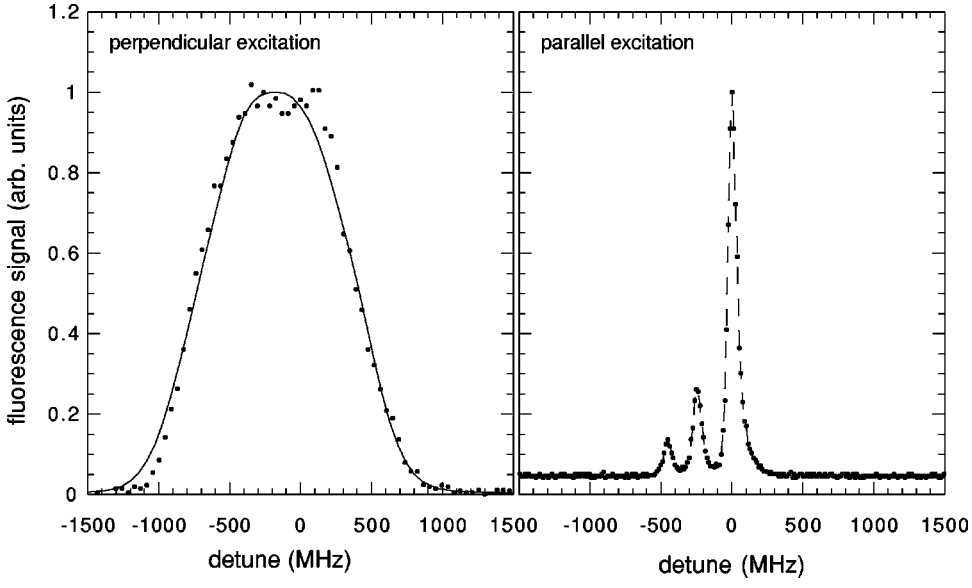

FIG. 5. Fluorescence vs laser frequency for both perpendicular and parallel excitation of the Cs $6s\,^2S_{1/2}F=4\rightarrow 6p\,^2P_{3/2}F'=3,4,5$ transitions in the fast beam. Perpendicularly excited, the spectral width is dominated by the transverse velocity distribution with a FWHM of 1.15 GHz. The solid line is the calculated line shape. For parallel excitation, the spectral width is dominated by the laser linewidth, and the dashed line is simply a guide to the eye.

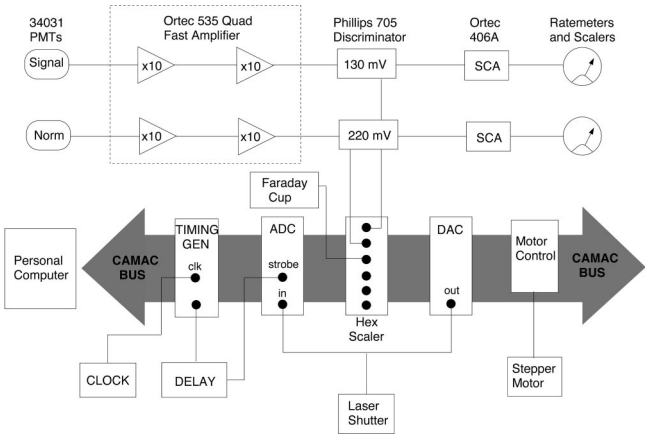

FIG. 6. Schematic of electronics setup for decay fluorescence observations. Front end amplifiers, discriminators, and analyzers are located in a NIM-type bin; modules on the CAMAC bus are in a separate crate.

beam. Two integration periods elapse at each position, one with laser shutter open and the second with the laser shutter closed. This procedure allows us to subtract the background due to residual gas excitation by the atomic and/or ion beam.

After a set of twelve translations is completed, the ion beam is blocked and two translating scans are recorded to acquire backgrounds due to scattered light from the excitation laser and dark counts. Because the diode lasers have an intensity stability of better than one part in 10^3 for the time intervals of interest, the laser-scattered light measurements are accurate even though they are not recorded in coincidence with the decay measurements. With the atomic beam unblocked and the decay detectors idling at a few hundred V, a velocity measurement is performed. The velocity laser is unblocked, and the wavelength of the Doppler shifted $D2$ resonance is recorded along with the unshifted resonance wavelength from a cesium cell. The platform voltage, as sensed by a differential voltmeter, is also recorded signifying beam velocity changes between Doppler-shift measurements. We then repeat the sequence of 12 decay scans, two background scans, and one velocity measurement for as long as the source remains operational.

A total of 23 decay curves, four background scans, and two velocity measurements were acquired for excitation to the $6p\,^2P_{3/2}$ state. For excitation to the $6p\,^2P_{1/2}$ state, 35 decays, six background scans, and three velocity measurements were recorded. Of these data sets, five $P_{3/2}$ and two $P_{1/2}$ decay scans suffered from ion source instabilities and were excluded from the analysis.

TABLE I. Typical beam parameters and signal rates for the fast-beam lifetime measurements.

Typical operating parameters Quantity	Size
Platform voltage	50.2 kV
Total analyzed Cs^+ current	18 μA
Neutral Cs current through chamber	2 μA
Residual ion current through chamber	150 nA
$P_{3/2}$ signal count rate (start of decay curve)	70 kHz
$P_{3/2}$ normalization count rate	80 kHz
$P_{1/2}$ signal count rate (start of decay curve)	3.5 kHz
$P_{1/2}$ normalization count rate	6 kHz
Beam velocity	2.7×10^7 cm/s

VIII. BACKGROUND SUBTRACTION

The total photon-counting rates in the signal photomultiplier $\mathcal{S}$ and in the normalizing photomultiplier $\mathcal{N}$ with both the atomic beam and exciting laser radiation present are a composite of rates due to the decay fluorescence and noise sources:

$$\mathcal{S}^{\text{laser}}_{\text{atoms}}(z,t)=S(z,t)+l(z)+b(z,t)+d(t), \tag{7}$$

$$\mathcal{N}^{\text{laser}}_{\text{atoms}}(z,t)=N(t)+l'(z)+b'(z,t)+d'(t), \tag{8}$$

where S and N are the true fluorescence signal and normalization count rates, and l, b, and d refer to background counts due to scattered laser radiation, beam-residual gas excitation, and detector dark counts. The decay signal and laser scatter in the translating detector are in general functions of position z, and the primes refer to the fact that the backgrounds are different in the two phototubes due to differing efficiencies, positions, etc. The time dependence due to fluctuations in each of these signal components is included explicitly. The apparent z dependence of $\mathcal{N}$ comes from the fact that the beam background b' can change during the time it takes to move the detector through its various positions. The laser scatter is treated only as a function of position and not of time because of the excellent intensity stability of the diode lasers. At short time intervals (10 s) we shutter the excitation laser, and count $\mathcal{S}$ and $\mathcal{N}$ with only the atomic beam present:

$$\mathcal{S}_{\text{atoms}}(z,t')=b(z,t')+d(t'), \tag{9}$$

$$\mathcal{N}_{\text{atoms}}(z,t')=b'(z,t')+d'(t'). \tag{10}$$

At longer time intervals, scans with the atomic beam blocked are taken, and the counting rates arise from the following contributions:

$$\mathcal{S}^{\text{laser}}(z,t'')=l(z)+d(t''), \tag{11}$$

$$\mathcal{N}^{\text{laser}}(z,t'')=l'(z)+d'(t'') \tag{12}$$

and

$$\mathcal{S}(z,t''')=d(t'''), \tag{13}$$

$$\mathcal{N}(z,t''')=d'(t'''). \tag{14}$$

To extract the true normalized decay signal S/N, we make the following subtraction:

$$\frac{S}{N}=\frac{[\mathcal{S}^{\text{laser}}_{\text{atoms}}-\mathcal{S}_{\text{atoms}}]-[\mathcal{S}^{\text{laser}}-\mathcal{S}]}{[\mathcal{N}^{\text{laser}}_{\text{atoms}}-\mathcal{N}_{\text{atoms}}]-[\mathcal{N}^{\text{laser}}-\mathcal{N}]}. \tag{15}$$

This subtraction is exact in the limit where the integrated beam current in two consecutive 10-s intervals is constant $[b(z,t)=b(z,t')]$ and where the dark counts are similarly stable $[d(t)=d(t')$ and $d(t'')=d(t''')]$. The dark counts are stable to within a few percent over a period of hours, depend-

TABLE II. Typical photon count rates due to true fluorescence and noise components.

	Photon count rate contributions	
	$6p\,^2P_{3/2}$	$6p\,^2P_{1/2}$
Decay fluorescence	8.7×10^4 Hz	4.6×10^3 Hz
Beam-gas excitation	2.3×10^3 Hz	1.4×10^3 Hz
Laser scattered light	25 Hz	10 Hz
Thermal (dark) noise	50 Hz	450 Hz

TABLE III. Shifted resonance positions and corresponding velocities measured during the experiment.

	Beam velocity measurements	
	Beam resonance	velocity
$P_{1/2}$ No. 1	11721.59(1) cm^{-1}	$2.7022(36)\times10^7$ cm/s
$P_{1/2}$ No. 2	11721.59(1) cm^{-1}	$2.7022(36)\times10^7$ cm/s
$P_{1/2}$ No. 3	11721.60(1) cm^{-1}	$2.6996(36)\times10^7$ cm/s
$P_{3/2}$ No. 1	11721.89(1) cm^{-1}	$2.7039(36)\times10^7$ cm/s
$P_{3/2}$ No. 2	11721.89(1) cm^{-1}	$2.7065(36)\times10^7$ cm/s

ing primarily on the temperature and conditioning of the tubes. A small background is due to beam excitation of the residual gas in the chamber; thus ion source stability is an important issue. The beam background subtraction may not be exact if the ion source output fluctuates during the 10-s interval between the observations at t and t'. We therefore discard sweeps with large particle current fluctuations which might destroy the integrity of the subtraction. The relative sizes of the various signal components are tabulated in Table II. A plot of the data recorded for a typical $6p\,^2P_{3/2}$ decay sweep with laser chopping is shown in Fig. 7.

Five velocity measurements are performed during the course of the experiment, three during $P_{1/2}$ data collection and two during the $P_{3/2}$ measurements. The scanning wavemeter is calibrated using the cesium vapor cell, and the fluorescence peaks corresponding to the $6s\,^2S_{1/2}F=3,4 \rightarrow 6p\,^2P_{3/2}F'=2,3,4,5$ transitions are found to have centers of gravity at 11732.16(1) cm^{-1} ($F=4$ ground state) and 11732.47(1) cm^{-1} ($F=3$ ground state). The velocity probe was driven from the ground state $F=4$ for the $P_{1/2}$ measurements and from $F=3$ for the $P_{3/2}$ measurements. The upper-state hyperfine structure is resolved in the fast-beam resonance, and we record the wavelength of the peak corresponding to total angular momentum $F=4$.

The results of the five velocity measurements are listed in Table III. Platform voltage stability is excellent, with fluctuations $<2\times10^{-4}$ which corresponds to the limiting accuracy of the divider and differential voltmeter used to obtain the voltage. The uncertainty in determining the velocity is dominated by the wavemeter precision of ±0.010 cm^{-1}, which yields a corresponding velocity uncertainty of $\pm0.0036\times10^7$ cm/s, or $\pm0.13\%$. The statistical spread of the several measurements is less than the wavemeter resolu-

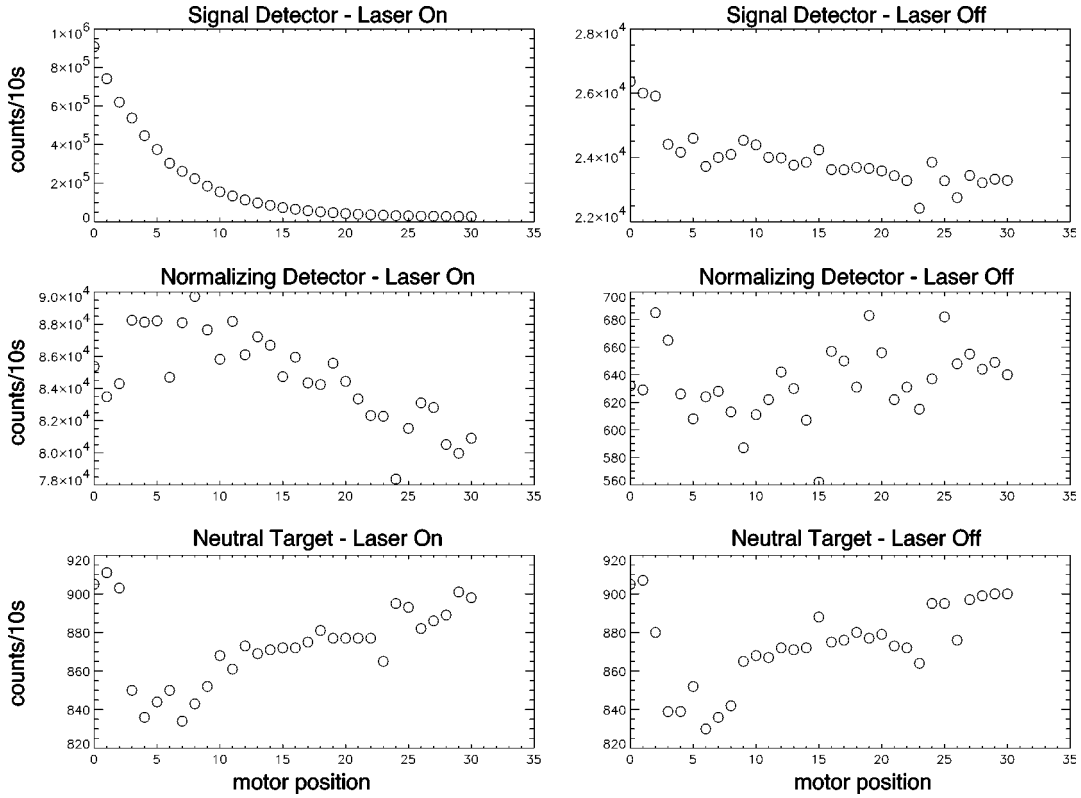

FIG. 7. Signals recorded during a typical downstream lifetime scan with excitation to the $6p\,^2P_{3/2}$ state and laser chopping. The horizontal axis is the detector position, and the vertical axis is the number of counts in 10 s. Position 30 corresponds to a maximum travel of 4.76 cm.

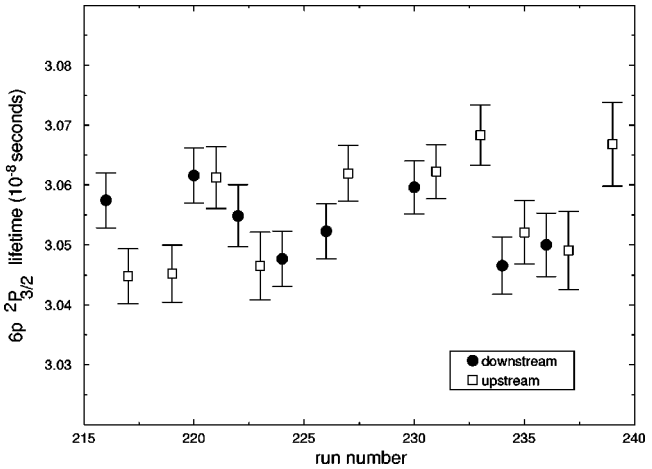

FIG. 8. Scatter plot of $6p\,^2P_{3/2}$ lifetimes obtained from full fits to individual data sets. Solid circles are runs acquired with the detector block translating downstream relative to the atomic beam, and open squares are acquired translating upstream.

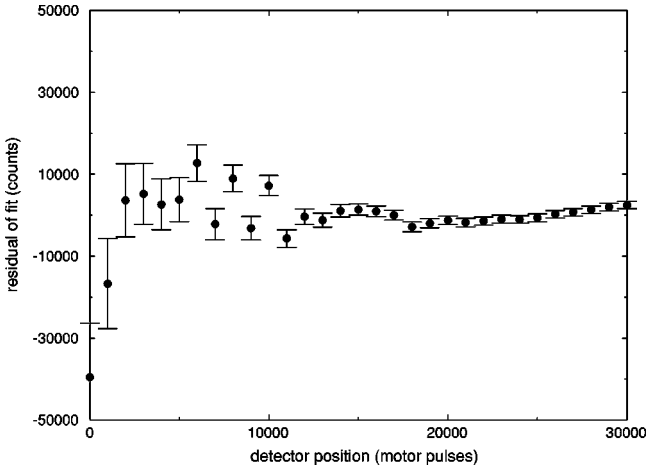

FIG. 9. Residuals of fit to sum of all $6p\,^2P_{3/2}$ decay data sets, out of a total number of 1.4×10^7 counts in the peak position. Error bars represent the total statistical error in each value, determined from the counting error in each detector propagated through the subtraction scheme. The last position corresponds to a maximum travel of 4.76 cm.

tion indicating the long-term stability of the beam velocity.

IX. FITTING PROCEDURE AND RESULTS

The background-subtracted normalized intensity data are fit to a single decaying exponential with arbitrary amplitude and a constant background

$$I(z)=I(z_0)\exp(-a_J z)+C, \tag{16}$$

where the lifetime τ_J is related to the spatial decay constant a_J via the beam velocity v:

$$\tau_J=\frac{1}{a_J v}. \tag{17}$$

Fitting is performed via minimization of the χ^2 parameter using the modified Levenberg-Marquardt scheme coded in a FORTRAN subroutine MRQMIN [19].

A. $6p\,^2P_{3/2}$ state lifetime

For excitation to the $6p\,^2P_{3/2}$ state, we fit 18 decay curves and determine $\tau_{3/2}$ using a velocity of $2.7052(36)\times10^7$ cm/s. This velocity is an average of the two measurements performed during the experimental run for this state; they are indistinguishable within the limits imposed by the wavemeter accuracy. Figure 8 illustrates the distribution of lifetimes measured for the 18 runs fit with all 31 detector positions included. No systematic discrepancy is observed between values obtained for upstream and downstream translations.

There are several possible systematic effects that could potentially shift the lifetime value obtained by the fitting algorithm. To make small effects statistically significant, we combine the data from all runs into a single ''superset.'' Figure 9 shows the residuals of the best fit to this superset. There are nonstatistical fluctuations clearly visible in the residuals that can manifest themselves as shifts in the fitted value of the lifetime when subsets of the data are fitted independently.

The effect which generates the most concern is inaccuracy in determining any residual constant background. It is found that fits to successive truncations of the superset generate differing values for the constant background. We therefore require that the background be chosen so that the fitted value of the lifetime remains within statistical fluctuations as successive truncations are performed. The second most important systematic effect in fitting has its origins in possible saturation of the detection system and/or counting electronics. If saturation is present, the signal will be artificially lower near the peak value of the decay curve, resulting in a fitted lifetime which is artificially long. As the data set is truncated, however, saturation effects are eliminated and the fitted lifetime converges to the actual value. Because a decay curve with saturation present is not a pure exponential, the background value obtained from the fit could be inaccurate. To illustrate this point, the dependence of the fitted value of the lifetime on truncation of the $6p\,^2P_{3/2}$ decay superset is plotted in Fig. 10 for three different values of the constant background.

A saturationlike effect does appear to be present, evidenced by a monotonic decrease in the fitted lifetime as points at the start of the decay are successively truncated. However, the saturationlike effect disappears by the time the first six or seven points have been dropped. The fitted value of the lifetime for large truncations depends on a proper choice of the background. The square plotting symbols show a decreasing lifetime over the entire range of truncations (up to 15 of the 31 points), indicating an overestimate of the background value when fitting the entire set. This overestimate can occur due to the presence of saturation at short times. Alternatively, the diamond symbols show an increasing lifetime with truncation when the background is set to zero, indicating that zero is an underestimate of the background and that the subtraction given in Eq. (15) may be incomplete. Some background is indeed present, and the circles illustrate the truncation behavior when a reasonable value for the background is chosen. Saturation is still evident, but the lifetime stabilizes after the saturated portion of

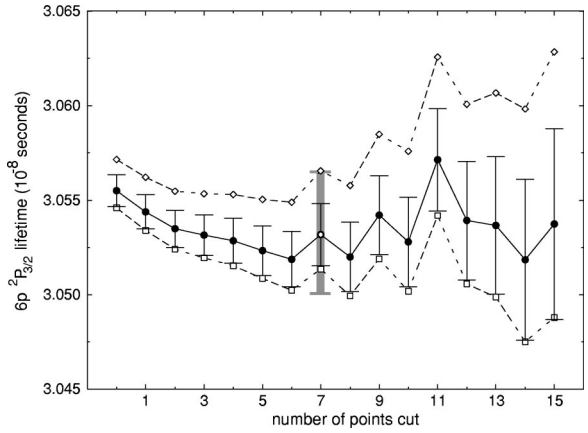

FIG. 10. Dependence of fitted lifetime on number of points truncated from the start of decay curve. Diamond symbols represent results obtained with zero background, squares results using the best-fit background for the entire (untruncated) data set, and circles results using the background value most stable against truncations. The hollow circle at seven points cut is taken to be the best value for $\tau_{3/2}$. Fine error bars represent the statistical error in fitting; the thick bar on the hollow circle illustrates the total fit reproducibility estimate (see text for details). Lines are intended only as a guide to the eye.

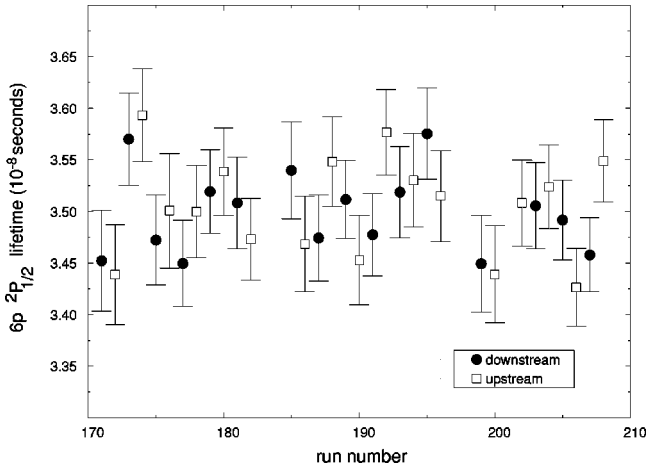

FIG. 11. Scatter plot of $6p\,^2P_{1/2}$ lifetimes obtained from full fits to individual data sets. Solid circles are runs acquired with the detector block translating downstream relative to the atomic beam, and open squares are acquired translating upstream.

the curve is truncated. Statistical fluctuations dominate after additional points are dropped from the dataset.

Because there is this saturationlike effect present at the beginning of the $6p\,^2P_{3/2}$ decay curve, we truncate the first seven points before determining our lifetime value. Through this procedure, we are effectively keeping the count rates sufficiently low to eliminate the need for dead time corrections. It is evident from Fig. 10 that the saturation effect is no longer significant at this signal level. The value of the lifetime $\tau_{3/2}$ obtained is 30.532 ns, with a statistical error in fitting of ± 0.016 ns. The uncertainty in the background estimate also contributes independently to the error in determining $\tau_{3/2}$ from the decay curve. A conservative estimate of ± 0.026 ns spans the interval of lifetimes from that obtained with no background to that obtained with the overestimated background of the untruncated fit. Combining these in quadrature yields the error in the fitting process, which contributes a total uncertainty of ± 0.031 ns or $\pm 0.10\%$ to the lifetime.

It is improbable that some of the nonstatistical fluctuations are due to quantum interference effects arising from partially selective excitation of the upper-state hyperfine structure and associated magnetic sublevels. Such quantum beats would be small in amplitude, because our detection system is polarization insensitive and the laser is linearly polarized perpendicular to the observation direction. Beat frequencies between hyperfine levels range from 150 to 250 MHz, more than an order of magnitude larger than the inverse observation time of our system. Therefore such beats are further reduced in our apparatus due to intrinsic averaging. Zeeman quantum beats between magnetic sublevels of the same hyperfine state occur only in the presence of a magnetic field. We measured the field in our apparatus to be <0.05 G at all points in the decay region. Such a field could give rise to very low-frequency quantum beats only in the presence of laser-induced orientation which is small in our system.

The residuals of the superset fit (Fig. 9) are frequency analyzed by performing a Fourier spectral decomposition of a cubic spline interpolation. Interpolation is necessary to obtain a meaningful fast Fourier transform. The spectral density shows five broad peaks centered at 15.7, 12.6, 7.3, 4.5, and 2.7 MHz. We then fit the data with these fixed beat frequencies to obtain their amplitudes and find the higher frequencies to be dominant. These frequencies are about 100 times lower than the physically allowed hyperfine quantum beats, and could only correspond to Zeeman beats that would occur in the presence of a magnetic field about 100 times larger than the residual field present in our system.

To estimate the uncertainty in our final result, we subtract the modulations, and refit the data. The lifetime thus obtained is 30.517(12) ns, slightly smaller but entirely consistent with the result from the truncation analysis. The resulting shift of -0.015 ns or 0.05% is taken as a separate estimate of the uncertainty in obtaining the lifetime due to these modulation effects. We regard this as a conservative estimate of the uncertainty, because the majority of this effect is eliminated by the trucation analysis since the apparent modulations are statistically insignificant after the first few detector positions.

B. $6p\,^2P_{1/2}$ state lifetime

For excitation to the $6p\,^2P_{1/2}$ state, 33 decay curves are analyzed with a velocity of $2.7013(36)\times 10^7$ cm/s. As above, the velocity used is the average of the three measurements performed during the experimental run in which $6p\,^2P_{1/2}$ decays are recorded. Figure 11 shows the distribution of lifetimes obtained for the full fits with all 31 detector positions included.

The truncation analysis is also performed for the $6p\,^2P_{1/2}$ state. None of the saturation or quantum-beat-like effects are observed in the $P_{1/2}$ decays, and the background obtained from the untruncated fit to the sum of all decays is found from the outset to be accurate with regard to our criterion of

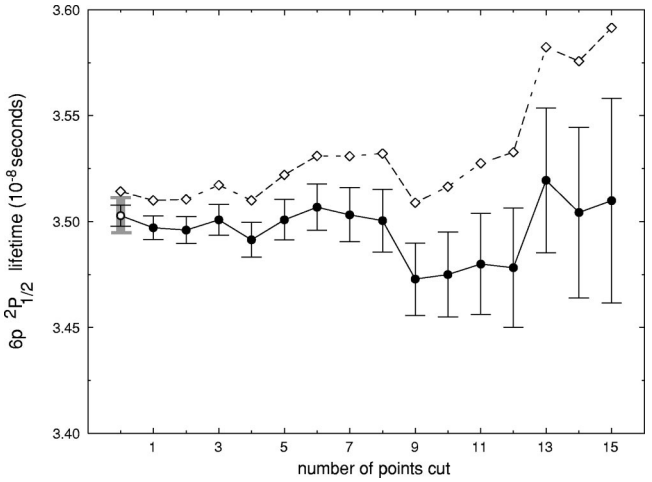

FIG. 12. Dependence of the fitted lifetime on the number of points truncated from the start of the decay curve. Diamond symbols are obtained with zero background, and circles using the background value most stable against truncations. The hollow circle with no points cut is taken to be the best value for $\tau_{1/2}$. Fine error bars represent the statistical error in fitting; the thick bar on the hollow circle is the total fit reproducibility estimate including background determination. Lines are intended only as a guide to the eye.

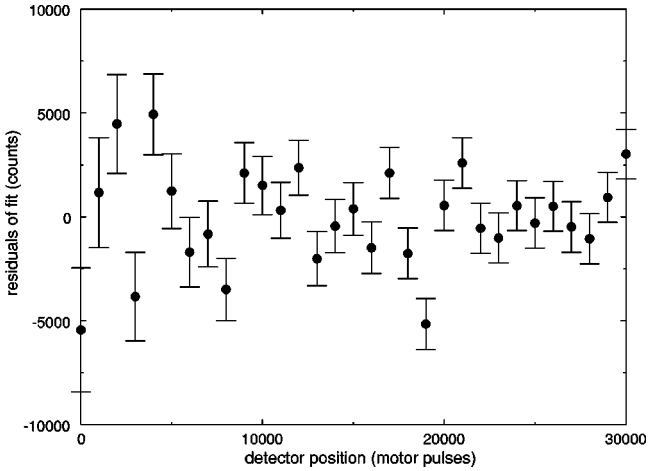

FIG. 13. Residuals of fit to sum of all $6p\ ^2P_{1/2}$ decay data sets, out of a total number of 1.3×10^6 counts in the peak position. Error bars represent the total statistical error in each value, determined from the counting error in each detector propagated through the subtraction scheme. The last position corresponds to a maximum travel of 4.76 cm.

returning a lifetime value which is stable against successive cuts (Fig. 12).

Because of the limited excitation and detection efficiencies at 894 nm, the peak photon count rate is smaller by about a factor of 20 in the case of the $P_{1/2}$ measurements. In the $P_{3/2}$ truncation analysis, the saturation effect disappears after the fluorescence has decayed to about 25% of the peak value; since the same counting electronics are employed in both measurements, a saturation effect due to electronics limitations should not appear in the $P_{1/2}$ data. In addition, quantum beats are not likely to appear in the $P_{1/2}$ decays, because the upper-state hyperfine levels have equal and opposite gyromagnetic factors which suppress the modulation. Because the absence of both saturation and quantum beats in the $P_{1/2}$ data is entirely expected, we cannot use the $P_{1/2}$ data either to confirm or eliminate either mechanism as the possible source of the non-statistical fluctuations in the $P_{3/2}$ analysis.

The residuals of the full fit to the summed superset of $6p\ ^2P_{1/2}$ decay data are plotted in Fig. 13. The best-fit lifetime is 35.028(75) ns, where the uncertainty includes a contribution of ±0.050 ns for statistical error in fitting and ±0.056 ns arising from uncertainty in determining the correct background.

X. SYSTEMATIC UNCERTAINTIES AND CORRECTIONS

A number of other systematic effects must also be considered. They arise from mechanical precision, background fluctuations, alignment of the translation system, and atomic beam divergence.

A. Mechanical precision

Imperfections in the precision lead screw, backlash in the gear train and rotary feedthrough, and stepper motor nonlinearity can contribute to the uncertainty in the exact position of the translating detector. Using the lead screw manufacturer's absolute maximum deviation figure, the translation error is calculated to be at most $\pm0.013\%$ of the total travel. Free play is eliminated from the gear train, and the motor holding torque eliminates gear backlash. However, the vacuum feedthrough permits $\approx2°$ of free play when measured with a load larger than that imposed by the translation stage giving a conservative upper estimate of the error as $\pm0.006\%$ over the total travel. We also include an additional uncertainty of $\pm1.8°$ equal to one full step of the motor giving $\pm0.006\%$. Combined, the total uncertainty in the lifetime due to potential mechanical nonlinearity is therefore estimated to be $\pm0.016\%$.

B. Background fluctuations

Background fluctuations occurring on time scales shorter than the intervals at which the backgrounds are measured can result in an imperfect subtraction. The most significant contribution comes from fluctuations in the beam background, which results from the excitation of neutral and ionic species in the detection region as the fast beam collides with residual gas atoms in the chamber. This effect is tied to the residual gas pressure in the chamber ($<10^{-7}$ torr). The large pumping volume and the several pumps which maintain the chamber and beamline vacuum serve to keep the pressure stable; however, monotonic changes in the beam backgrounds are observed over the course of single runs which do not track with the measured particle current. The subtraction error is related to the curvature of the beam background. As a function of position (i.e., data collection time), the measured evolution of the beam background is largely linear; hence the primary effect is the addition of a constant error (proportional to the first derivative of the background evolution) for which we compensated with the constant background parameter in the fits. We also analyze the beam background data for higher-order curvatures which appear as a position-dependent background subtraction error, and an upper limit

of ± 0.4 Hz/channel is estimated for the drift in the $6p\,^2P_{1/2}$ decays. This drift changes the effective lifetime of the $P_{1/2}$ state by approximately $\pm 0.05\%$. Since the beam background increases and decreases randomly from run to run, the effect is expected to be much less important when all data sets are combined. Our estimate of the subtraction error due to beam background fluctuations is approximately the same for the $6p\,^2P_{3/2}$ measurements; but since the true fluorescence rate is ≈ 20 times larger for $6p\,^2P_{3/2}$, the fractional uncertainty is smaller by this factor, giving $\pm 0.003\%$.

Laser power fluctuations are a negligible contribution to the background subtraction error since we are using diode lasers. The light power is stable to $\pm 0.1\%$ over the course of a run, and the normalization system accounts well for any fluctuations. Laser scatter contributes less than 0.03% to the total photon count rate, so small fluctuations in this background are unimportant. Therefore, a conservative addition to the error budget of $\pm 0.05\%$ for both decay measurements more than covers all uncertainties in the background subtraction scheme.

C. Tracking error

If the fast atomic beam and direction of translation of the detector are not exactly parallel, changes in the collection solid angle can occur as the detector is translated. This effect could cause a systematic error in the lifetime value extracted from the data depending on whether the collection probability increases or decreases as the detector translates down the beam. Apertures on the lid, and the upstream aperture of the charge exchange cell define the atomic beam direction. The lid apertures are carefully aligned so that the beam path is constrained to be parallel to the translation direction within ± 100 μm over the 4.76-cm travel length. The lid apertures are then aligned with those of the charge exchange cell by sighting down the beamline with a telescope while adjusting the location of the lid and/or charge exchange cell.

To determine the possible uncertainty in the collection solid angle due to mistracking, we calculate the detection efficiency as a function of the displacement of the detector assembly in the horizontal and vertical planes. Using a Monte Carlo scheme, we calculate the signal amplitude per atom as a function of the rectangular coordinates (a_i,b_i,c_i) of the ith fiber bundle (there are two). The signal amplitude per atom S into the bundle at position z_0 is the integral of the excited state population density of the atomic beam times the geometrical solid angle, normalized for decay and the number of atoms in the integration length. For a beam of particle current I propagating in the z direction with speed v,

$$S(z_0)=\int\int\int \frac{I}{v}\,\frac{e^{-(z+z_0)/v\tau}}{\pi[\phi(z+z_0)+r_0]^2}\,\Omega(x,y,z)\,dx\,dy\,dz, \tag{18}$$

where (x,y,z) range over the beam volume, ϕ is the half-angle of beam divergence, r_0 is the initial beam radius, and z_0 is the bundle position. The total solid angle subtended by the two bundles is given by

$$\Omega(x,y,z)=\sum_{i=1}^{2}\int_{face}\frac{\hat{R}_i\cdot\hat{n}_i}{4\pi R_i^2}\,da_i\,db_i, \tag{19}$$

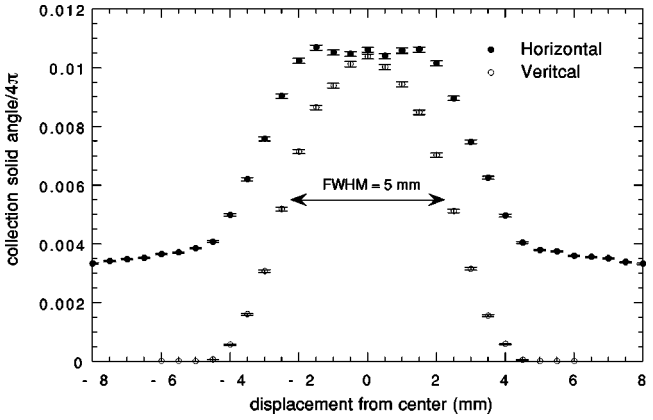

FIG. 14. Calculated collection efficiency for various displacements of the detector block in the horizontal and vertical planes, perpendicular to the beam axis. Error bars represent the uncertainty in the stochastic integration. Placing the two fiber bundles facing each other in the horizontal direction decreases the sensitivity to translation in this direction, as evidenced by the flat top of the curve.

where $\vec{R}_i$ is the relative position vector from the source atom to a point (a_i,b_i,c_i) on the bundle face, and $\hat{n}_i$ is the unit vector normal to that face. The integral ranges over the area of the bundle face. The normal dot product can be written in terms of the fiber bundle coordinates using the relation

$$\hat{R}_i\cdot\hat{n}_i=\frac{b_i-y}{\sqrt{(a_i-x)^2+(b_i-y)^2+(c_i-z)^2}}. \tag{20}$$

Performing the numerical integration with z_0 fixed, we calculate the collection solid angle. A numerical cutoff eliminates rays that enter the fibers at angles larger than the acceptance angle. The integration is repeated as a function of vertical (x) and horizontal (y) displacement of the bundles, and the results are shown in Fig. 14.

Because the fibers have such large acceptance angles and are mounted face-to-face in the horizontal direction, the apparatus is relatively insensitive to tracking error in the horizontal plane (Fig. 14), even for displacements as large as 2 mm. In the vertical plane (Fig. 14), the apparatus is more sensitive to mistracking, with a calculated fractional signal change of 3.8×10^{-5} per μm of displacement from center (for displacements $\leqslant 300$ μm). Taking the maximum anticipated tracking error from the combined alignment uncertainties to be ± 200 μm, the maximum possible deviation from true exponential behavior due to mistracking is $\pm 1.6\times 10^{-4}$ mm^{-1}. Multiplying by $v\tau$ [see Eq. (23) below], this introduces an uncertainty of $\pm 0.13\%$ in the lifetime value.

D. Correction for beam divergence

Spreading of the atomic beam as it traverses the detection region can also lead to changes in the collection solid angle resulting in systematic shifts in the apparent lifetime. Volz *et al.* [20] investigated the divergence of a charged helium beam using beam profile monitors. Assuming that the profile of the neutralized helium could be inferred from measurements of the ion-beam profile, the authors used a geometrical

factor $C_{\rm div}$ to correct measured lifetimes $\tau_{\rm meas}$ in neutral helium to the true lifetimes τ via the relation

$$\frac{1}{v\tau_{\rm meas}}=\frac{1}{v\tau}+C_{\rm div}. \tag{21}$$

$C_{\rm div}$ is a constant specific to the detection system which parameterizes the change in detection probability for photons emitted by atoms in the diverging beam as the detector translates along. $C_{\rm div}$ can be estimated from the spatial dependence of the collection efficiency; assuming an elliptical Gaussian atomic beam overlapping an elliptical Gaussian detection window [20],

$$C_{\rm div}=\frac{a_0}{a_0^2+w_x^2}\delta_x+\frac{b_0}{b_0^2+w_y^2}\delta_y, \tag{22}$$

where a_0, b_0 are the lengths of the major and minor axes of the beam at the start position, $w_{x,y}$ are the full widths at half maximum (FWHM) of the collection efficiencies of the detector, and $\delta_{x,y}$ are the divergence half-angles projected onto the horizontal and vertical planes. The authors verified this approach for divergence correction by comparing experimental lifetimes with theoretical calculations that were expected to be accurate for neutral helium [3].

Transverse excitation of the fast beam resonance directly reveals the effects of beam divergence. Figure 5 shows the fluorescence spectra obtained for both transverse and longitudinal excitation. We model the line shape for transverse excitation, taking into account several broadening mechanisms: the measured laser linewidth, natural linewidth, saturation of the transition, finite transit time through the excitation region, and the transverse velocity distribution of the atomic beam. Modeling the line profile (the solid line in Fig. 5) reveals that the majority of the broadening results from the transverse velocity distribution. Our model distribution is derived from the geometrically allowed velocities projected along the laser direction. The velocity directions are limited before entering the detection region by two 3.2-mm-diameter apertures separated by 2.0 m, permitting a maximum divergence half-angle of 1.6 mrad. The agreement between the observed spectrum and the model verifies this geometrical limitation.

To correct for beam divergence effects in the lifetime, we use several approaches. First, we use the spatial dependences of the detection efficiencies, shown in Fig. 14, and apply Eq. (22). Our detection efficiency is flat for changes $<\pm 2$ mm in the horizontal (y) direction, and since the beam does not diverge outside this interval the second term is negligible for our apparatus. The atomic beam has a diameter of $a_0=3.2$ mm, and the laser excitation is uniform in the x direction because the laser propagates vertically. Using the FWHM of $w_x=5$ mm from Fig. 14, and the divergence angle $\delta_x=1.6$ mrad, we find

$$C_{\rm div}=1.45\times 10^{-4}\ \ {\rm mm}^{-1}. \tag{23}$$

We also determine the divergence correction by an independent approach. Using our geometrical constraints, we numerically integrate over the expanding beam volume using Eq. (18), thus calculating the fractional signal change as a function of translation distance. We obtain the result

$$C_{\rm div}=1.58\times 10^{-4}\ \ {\rm mm}^{-1}. \tag{24}$$

As another test of our numerical integration, we also calculated $C_{\rm div}$ by explicitly differentiating Eq. (18) with respect to detector position and integrating numerically.

We use the average of Eqs. (23) and (24) and conservatively estimate the uncertainty in $C_{\rm div}$ to be 50% due to uncertainties in the divergence, geometry, and integration scheme, although the consistency of the two methods suggests that the values might be more trustworthy. From Eq. (21), the correction to the lifetime is found to be

$$\tau=\tau_{\rm meas}\left(1+\frac{\tau_{\rm meas}vC_{\rm div}}{1-\tau_{\rm meas}vC_{\rm div}}\right). \tag{25}$$

Hence the lifetime values must be corrected toward longer values by $+0.12\%$ with $\pm 0.06\%$ for the uncertainty in $C_{\rm div}$.

TABLE IV. Summary of contributions to uncertainty in lifetime measurements.

	Lifetime error budget	
	$6p\,^2P_{3/2}$	$6p\,^2P_{1/2}$
Beam velocity	0.13%	0.13%
Fit reproducibility	0.10%	0.21%
Quantum beats	0.05%	0
Mechanical	0.016%	0.016%
Background drift	0.05%	0.05%
Mistracking	0.13%	0.13%
Beam divergence	0.06%	0.06%
Total uncertainty	0.23%	0.29%

XI. RESULTS

The complete error budget is summarized in Table IV. The final lifetime results, including divergence corrections, are 30.57(7) ns for the $6p\,^2P_{3/2}$ state, and 35.07(10) ns for the $6p\,^2P_{1/2}$ state. The ultimate precision is $\pm 0.23\%$ in the $P_{3/2}$ lifetime and $\pm 0.29\%$ in the $P_{1/2}$ lifetime. The lifetimes appearing in the present paper are slightly longer than our previously published values [5] due primarily to the inclusion of beam divergence effects. The work presented here represents a larger data set along with a comprehensive description of the apparatus and procedures used for data analysis.

Previous measurements and calculations of the $6p\,^2P_J$ lifetimes in cesium are compared with the present results in Table V. Experiments with uncertainties greater than 5% and those performed before 1960 have been excluded from the table; historical references can be found in Ref. [4].

Both fine-structure components are measured in only three experiments: the phase shift experiment of Dodd *et al.* [21], the time-correlated photon counting experiment of Young *et al.* [22], and the present work. Comparable uncertainties ($<1\%$) are quoted only for our first fast-beam measurement [4], the experiment of Young *et al.* [22], and the level crossing measurement of Rydberg and Svanberg [23].

TABLE V. Summary of empirical and calculated lifetimes obtained for the $6p\,^2P_{1/2,3/2}$ states of cesium.

Lifetime (ns)			
$6p\,^2P_{3/2}$ state	$6p\,^2P_{1/2}$ state	Method	Reference
30.57±0.07	35.07±0.10	fast-beam laser	This work
30.55±0.27		fast-beam laser	Tanner *et al.* [4]
30.41±0.10	34.75±0.07	time-resolved laser	Young *et al.* [22]
31.8±0.7		time-resolved laser	Campani and Salvo [35]
29.9±0.2		level crossing	Rydberg and Svanberg [23]
32.7±1.5		level crossing	Schmieder *et al.* [36]
30.8±1.5	35.2±1.5	phase shift	Dodd *et al.* [21]
30.5±0.7		phase shift	Link [37]
30.99	35.53	MBPT	Dzuba *et al.* [24]
30.49	34.92	energy corrected	Dzuba *et al.* [24]
30.81	35.22	MBPT	Blundell *et al.* [26]
30.13	34.51	energy corrected	Blundell and co-workers [25,26]
30.563	34.961	CAHS	Theodosiou [33]

The results presented here are in excellent agreement with our previous fast-beam measurement of the $6p\,^2P_{3/2}$ lifetime. Our present result for the $6p\,^2P_{3/2}$ state is in marginal agreement with the measurement of Young *et al.* [22], however the discrepancy of 0.5% is within the combined 1σ limit. For the $6p\,^2P_{1/2}$ state, our lifetime is 0.9% longer than that of Young *et al.* [22], which is nearly twice the combined 1σ uncertainty. We agree well with all other measurements except for that of Rydberg and Svanberg [23], which disagrees substantially with all of the newer precision measurements.

Two very accurate *ab initio* calculations exist for the $6p\,^2P_J$ lifetimes in cesium. Both apply relativistic many-body perturbation theory (MBPT) to the calculation of the electric dipole matrix elements for the two $6p\,^2P_J \rightarrow 6s\,^2S_{1/2}$ transitions; they differ in that certain contributions are not included in one or the other formulation. High-accuracy calculations which are truly *ab initio* are vital to the interpretation of atomic parity-nonconservation (PNC) measurements in cesium [7,8]. The calculation due to Dzuba *et al.* [24] is of the coupled-cluster type which includes three dominant classes of diagrams: screening of the residual electron-electron correlations, particle-hole interactions, and self-energy contributions. The most recent all-orders calculations of Blundell and co-workers [25,26] for cesium are comparable, including single and double excitations with an extension to include the effect of triple excitations on the singles coefficients. In cesium this subset of triple excitations is important and contributes significantly to the atomic structure starting at the level of third-order MBPT [25]. The differences between the calculations of Blundell and co-workers and Dzuba *et al.* are outlined in Ref. [25]. Figure 15 compares the best experimental results with these most accurate *ab initio* calculations. The resulting values for the transition matrix elements calculated from the two techniques differ from each other by 0.4% for the $6S_{1/2} \rightarrow 6P_{1/2}$ transition, and 0.3% for the $6S_{1/2} \rightarrow 6P_{3/2}$ transition. The transition probabilities or lifetimes, then, differ by 0.8% and 0.6% according to Eq. (1), which connects the lifetime of the single decay mode to the square of the reduced matrix element. Because a factor of the third power of the transition frequency appears in this expression, the conversion from matrix element to lifetime is quite sensitive to the transition energy. The MBPT transition energies [24–26] differ from precise experimental determinations [27–32] of the energy intervals by 0.5–0.8 %; therefore, transition probabilities rescaled with the experimental energies are also included in Table V and Fig. 15. This energy correction has the effect of decreasing the theoretical lifetime values by about 2%.

Our measured lifetimes show good agreement with the energy-corrected values derived from Ref. [24], but are 1.4% longer than the values obtained from Refs. [25,26]. The calculation of Ref. [24] does contain additional nonlinear contributions omitted entirely from Refs. [25,26], but agreement between experiment and the energy-corrected calculated lifetimes is not necessarily to be expected. This is because certain correlation effects have not yet been included in both calculations, and it is uncertain which classes of diagrams are the important ones at the fraction of a percent level. Indeed from the outset, our experimental program has been moti-

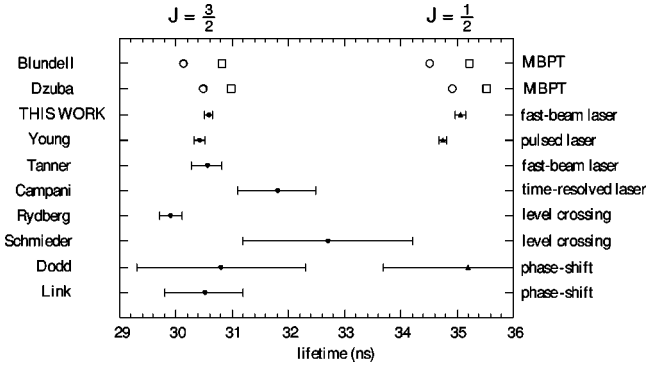

FIG. 15. Comparison of the best empirical lifetime values with calculations. Open squares are purely *ab initio* values, and open circles are scaled to experimental transition energies. Solid symbols represent experiment. See Link [37], Dodd *et al.* [21], Schmieder *et al.* [36], Rydberg and Svanberg [23], Campani and Salvo [35], Tanner [4], Young *et al.* [22], Dzuba *et al.* [24], and Blundell coworkers [25,26].

TABLE VI. $6S$-$6P$ reduced matrix elements in units of the Bohr radius a_∞. Phases are determined theoretically; the results of Ref. [24] have been scaled with geometric factors so that both calculations have identical normalization.

$\langle 6S_{1/2}\|\|r\|\|6P_J\rangle$ (a_∞)			
$J=3/2$	$J=1/2$	Method	Reference
−6.3238(73)	−4.4890(65)	fast-beam laser	This work
−6.3403(64)	−4.5097(74)	time-resolved laser	Young *et al.* [22]
−6.326(28)		fast-beam laser	Tanner *et al.* [4]
−6.30(15)	−4.48(19)	phase shift	Dodd *et al.* [21]
−6.332	−4.499	*ab initio*	Dzuba *et al.* [24]
−6.370	−4.525	*ab initio*	Blundell and co-workers [25,26]

vated by the need for precision measurements which can help to answer this question.

The comparisons between experiment and *ab initio* calculation may also be explored using the reduced matrix elements directly, which can be obtained from the lifetime data using Eq. (1). The results are tabulated in Table VI.

A semiempirical approach [33,34] for predicting lifetimes using the Coulomb approximation with a Hartree-Slater model potential for the core has also been used by Theodosiou [33] to find the lifetimes of the $6P_J$ states. The predicted lifetimes are based entirely on experimentally measured data for energy levels, ionization potentials, and core polarizabilities. The lifetimes predicted by this technique are also in very good agreement with the present measurements (Table V), but the accuracy of the method is difficult to assess. This procedure also lacks the physically interpretive power of *ab initio* methods, which is required for analysis of atomic PNC data.

The ratio of the reduced matrix elements derived from our lifetime measurements agrees well with a higher precision measurement of the $6\,^2S_{1/2}$–$6\,^2P_{3/2}$ to $6\,^2S_{1/2}$–$6\,^2P_{1/2}$ line strength ratio obtained through absorption measurements in our laboratory. A detailed comparison between measured ratios of line strengths and theoretical results for cesium and other alkalis appears in Refs. [3,9].

ACKNOWLEDGMENTS

We thank W. R. Johnson and J. Sapirstein for helpful discussions. We also thank M. F. Ifferte for assistance with the figures. This work was part of the doctoral thesis of R. J. R. at the University of Notre Dame, and he also thanks the Arthur J. Schmitt Foundation for support. Financial support for this work was provided by the Division of Chemical Sciences, Office of Basic Energy Sciences, Office of Energy Research at the U.S. Department of Energy under Contract No. DE-FG02-95ER14579 and No. DE-FG02-92ER14283.

[1] H. J. Andrä, A. Gaupp, and W. Wittmann, Phys. Rev. Lett. **31**, 501 (1973).
[2] A. Gaupp, P. Kuske, and H. J. Andrä, Phys. Rev. A **26**, 3351 (1982).
[3] U. Volz and H. Schmoranzer, Phys. Scr. **T65**, 48 (1996).
[4] C. E. Tanner, A. E. Livingston, R. J. Rafac, F. G. Serpa, K. W. Kukla, H. G. Berry, L. Young, and C. A. Kurtz, Phys. Rev. Lett. **69**, 2765 (1992).
[5] R. J. Rafac, C. E. Tanner, A. E. Livingston, K. W. Kukla, H. G. Berry, and C. A. Kurtz, Phys. Rev. A **50**, R1976 (1994).
[6] E. D. Commins and P. H. Bucksbaum, in *Weak Interactions of Leptons and Quarks*, 1st ed. (Cambridge University Press, Cambridge, England, 1983).
[7] C. S. Wood, Ph.D. thesis, University of Colorado, 1996 (unpublished).
[8] C. S. Wood, S. C. Bennett, D. Cho, B. P. Masterson, J. L. Roberts, C. E. Tanner, and C. E. Wieman, Science **275**, 1759 (1997).
[9] R. J. Rafac and C. E. Tanner, Phys. Rev. A **58**, 1087 (1998).
[10] R. E. Imhof and F. H. Read, Rep. Prog. Phys. **40**, 1 (1977).
[11] C. E. Tanner, in *Accelerator-Based Atomic Physics Techniques and Applications*, 1st ed. (AIP, New York, 1997), p. 609.
[12] K. O. Nielsen, Nucl. Instrum. **1**, 289 (1957).
[13] W. K. Brookshier, Argonne National Laboratory, Technical Report No. L7374-8602-DA (unpublished).
[14] *Physics Vade Mecum*, edited by H. L. Anderson (AIP, New York, 1981), p. 90.
[15] R. J. Rafac, Ph.D. thesis, University of Notre Dame, 1997 (unpublished).
[16] H. Schmoranzer, H. Roth, U. Volz, and D. Marger, J. Phys. B **24**, 595 (1991).
[17] U. Volz, M. Majerus, H. Liebel, A. Schmitt, and H. Schmoranzer, Phys. Rev. Lett. **76**, 2862 (1996).
[18] P. M. Koch, Opt. Commun. **20**, 115 (1977).
[19] W. H. Press, S. A. Teukolsky, W. T. Vetterling, and B. P. Flannery, *Numerical Recipes in FORTRAN*, 2nd ed. (Cambridge University Press, New York, 1992).
[20] U. Volz, D. Marger, H. Roth, and H. Schmoranzer, J. Phys. B **28**, 579 (1995).
[21] J. N. Dodd, E. Enemark, and A. Gallagher, J. Chem. Phys. **50**, 4838 (1969).
[22] L. Young, W. T. Hill III, S. J. Sibener, S. D. Price, C. E. Tanner, C. E. Wieman, and S. R. Leone, Phys. Rev. A **50**, 2174 (1994).
[23] S. Rydberg and S. Svanberg, Phys. Scr. **5**, 209 (1972).

[24] V. A. Dzuba, V. V. Flambaum, A. Y. Kraftmakher, and O. P. Shushkov, Phys. Lett. A **147**, 373 (1989).
[25] S. A. Blundell, W. R. Johnson, and J. Sapirstein, Phys. Rev. A **43**, 3407 (1991).
[26] S. A. Blundell, J. Sapirstein, and W. R. Johnson, Phys. Rev. D **45**, 1602 (1992).
[27] G. Avila, P. Gain, E. de Clercq, and P. Cerez, Metrologia **22**, 114 (1986).
[28] K. B. S. Eriksson and I. Wenaker, Phys. Scr. **1**, 21 (1970).
[29] R. J. Rafac and C. E. Tanner, Phys. Rev. A **56**, 1027 (1997).
[30] J. Abele, Z. Phys. A **274**, 185 (1975).
[31] C. E. Tanner and C. Wieman, Phys. Rev. A **38**, 1616 (1988).
[32] Th. Udem, J. Reichert, R. Holzwarth, and T. W. Hänsch, Phys. Rev. Lett. **82**, 3568 (1999).
[33] C. Theodosiou (private communication).
[34] L. J. Curtis, Phys. Scr. **48**, 559 (1993).
[35] E. Campani and R. D. Salvo, Lett. Nuovo Cimento **29**, 485 (1980).
[36] R. W. Schmieder, A. Lurio, W. Happer, and A. Khadjavi, Phys. Rev. A **2**, 1216 (1970).
[37] J. K. Link, J. Opt. Soc. Am. **56**, 1195 (1966).
[38] Defined by international agreement.